Dynamics of a surfactant-laden bubble bursting through an interface

C. R. Constante-Amores[1], L. Kahouadji[1], A. Batchvarov[1], S. Shin[2], J. Chergui[3], D. Juric[3] and O. K. Matar[1]†

[1]Department of Chemical Engineering, Imperial College London, London SW7 2AZ, UK

[2]Department of Mechanical and System Design Engineering, Hongik University, Seoul 121-791, Republic of Korea

[3]Laboratoire d'Informatique pour la Mécanique et les Sciences de l'Ingénieur (LIMSI), Centre National de la Recherche Scientifique (CNRS), Université Paris Saclay, Bât. 507, Rue du Belvédère, Campus Universitaire, 91405 Orsay, France

(Received xx; revised xx; accepted xx)

We study the effect of surfactant on the dynamics of a bubble bursting through an interface. We perform fully three-dimensional direct numerical simulations using a hybrid interface-tracking/level-set method accounting for surfactant-induced Marangoni stresses, sorption kinetics, and diffusive effects. We select an initial bubble shape corresponding to a large Laplace number and a vanishingly small Bond number in order to neglect gravity, and isolate the effects of surfactant on the flow. Our results demonstrate that the presence of surfactant affects the dynamics of the system through Marangoni-induced flow, driving motion from high to low concentration regions, which is responsible for the onset of a recirculation zone close to the free surface. These Marangoni stresses rigidify the interface, delay the cavity collapse, and influence the jet breakup process.

1. Introduction

When a bubble is resting close to a liquid-gas interface, its rupture gives rise to the formation of a central jet. This jet breaks up into small droplets, which could transport biological material, toxins, salts, surfactants or dissolved gases (Woodcock *et al.* 1953; MacIntyre 1972; Veron 2015; Zenit & Rodríguez-Rodríguez 2018; Séon & Liger-Belair 2017; Poulain & Bourouiba 2018). It is unsurprising therefore that the bursting bubble phenomena have received significant interest due to their occurrence in a multitude of natural and industrial applications. In the absence of contaminants, the physical mechanisms of surfactant-free bursting bubbles on the ejection of droplets have been widely studied experimentally (Woodcock *et al.* 1953; Ghabache *et al.* 2014; Ghabache & Séon 2016; Séon & Liger-Belair 2017), numerically (Deike *et al.* 2018; Gordillo & Rodríguez-Rodríguez 2019; Singh & Das 2019), and through theoretical approaches (Zeff *et al.* 2000; Gañán-Calvo 2017; Lai *et al.* 2018; Blanco-Rodrìguez & Gordillo 2020).

This previous work has shown that when a nucleated bubble rises through the liquid and then rests close to a free surface, its static resting shape results from a balance between gravitational and surface tension forces. The bubble shape may be characterised by a submerged interface, a liquid layer/cap above the bubble, and an interface, which extends away from the bubble cap (Toba 1959; Ghabache 2015). The cap is characterised by a length scale $\delta/R_o \sim O(10^{-6})$, where δ and R_o refer to the liquid layer thickness and the initial bubble radius, respectively. The layer curvature creates over-pressure relative

† Email address for correspondence: o.matar@imperial.ac.uk

to the liquid bulk below it. The fluid within the layer drains over time enabling van der Waals forces to rupture the interface when $\delta \to 0$ forming a hole (Lhuissier & Villermaux 2012). The hole leaves an open, unstable cavity that collapses to form a vertical jet whose dynamics are governed by inertial, viscous, and capillary forces.

Surfactants can affect the dynamics of surface-tension driven flows by the reduction of the local surface tension and capillary pressure, and by the formation of Marangoni stresses brought about by gradients in interfacial surfactant concentration. In a recent study, Constante-Amores *et al.* (2020) reviewed the state-of-the-art of the effect of surfactant in the dynamics of capillary singularities due to topological change. Craster *et al.* (2002) have shown that the presence of insoluble surfactant during the thinning of threads does not alter the well known breakup scalings predicted by Eggers (1993) as the capillary singularity is such a violent event which convects surfactant away from the pinchoff point. Both McGough & Basaran (2006) and Kamat *et al.* (2018) have reported that the presence of surfactant changes the fate of the thinning of threads as surfactant enhances the formation of micro-threads, whose thinning dynamics also follow Eggers (1993). Constante-Amores *et al.* (2020) showed that the presence of surfactant can suppress the 'end-pinching' mechanism in the retracting dynamics of ligament threads due to the suppression of stagnation points, and subsequent flow reversal. Most of chemical surfactants are soluble in the bulk liquid, adding a layer of complexity to the phenomena as Marangoni stress can also be regulated by the surfactant sorption kinetics between the bulk and interface. Liao *et al.* (2004) observed experimentally that high concentrations of soluble surfactant favour an asymmetric breakup of a liquid bridge. Jin *et al.* (2006), and Jin & Stebe (2007) showed that solubility affects the dynamics of drop formation in terms of thinning. Craster *et al.* (2009) have shown that similar to their previous work (Craster *et al.* 2002), the addition of solubility does not affect the scaling predicted by Eggers (1993), but it does lead to the formation of larger satellite droplets, which was confirmed experimentally by Kovalchuk *et al.* (2016, 2018).

As revealed by the foregoing review, studies involving surfactant effects on interfacial flows have received considerable attention, however, to the best of our knowledge, the influence of surfactants on the dynamics of bursting bubbles has not been explored, and this is the subject of the present article. Here, we use three-dimensional numerical simulations to account for surfactant solubility, diffusion, sorption kinetics, and Marangoni stresses on the bursting phenomena. The rest of this paper is structured as follows: in Section 2, the numerical method, governing dimensionless parameters, problem configuration, and validation, are introduced. Section 3 presents the results, and concluding remarks are given in Section 4.

2. Problem formulation and numerical method

The numerical simulations were performed by solving the two-phase Navier-Stokes equations in a three-dimensional Cartesian domain $\mathbf{x} = (x, y, z)$ (see figure 1). A hybrid front-tracking/level-set method was used to treat the interface, where surfactant transport was resolved both in the bulk and on the interface (Shin *et al.* 2018). Here, and in what follows, all variables will be made dimensionless (represented by tildes) using

$$\tilde{\mathbf{x}} = \frac{\mathbf{x}}{R_o}, \quad \tilde{t} = \frac{t}{T}, \quad \tilde{\mathbf{u}} = \frac{\mathbf{u}}{U}, \quad \tilde{p} = \frac{p}{\rho U^2}, \quad \tilde{\sigma} = \frac{\sigma}{\sigma_s}, \quad \tilde{\Gamma} = \frac{\Gamma}{\Gamma_\infty}, \quad \tilde{C} = \frac{C}{C_\infty}, \quad \tilde{C}_s = \frac{C_s}{C_\infty}, \tag{2.1}$$

where, t, $\mathbf{u}$, and p stand for time, velocity, and pressure, respectively. The physical parameters correspond to the liquid density ρ, viscosity, μ, surface tension, σ, surfactant-

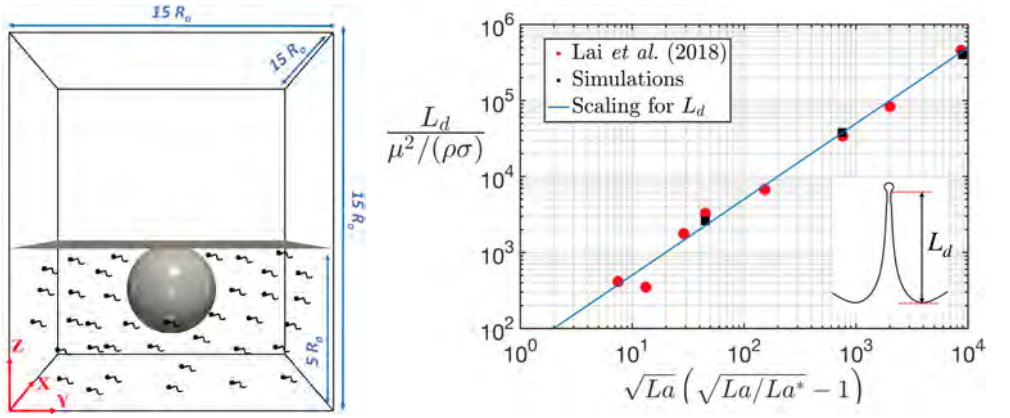

(a) (b)

FIGURE 1. (a) Initial shape of the bubble resting close to the interface, highlighting the computational domain of size $(15R_o)^3$ (not-to-scale) in a three-dimensional Cartesian domain $\mathbf{x} = (x, y, z)$, where Cartesian resolution is 768^3; (b) comparison of surfactant-free simulations from the current study (squares) with scaling argument of the length of the jet (solid line) and numerical simulations (dots) proposed by Lai *et al.* (2018).

free surface tension, σ_s, and gravitational acceleration, g; $T = \sqrt{\rho R_o^3/\sigma_s}$ is the capillary time scale, hence the velocity scale is $U = R_o/T = \sqrt{\sigma_s/(\rho R_o)}$. The interfacial surfactant concentration, Γ, is scaled on the saturation interfacial concentration, Γ_∞, whereas the bulk and bulk sub-phase (immediately adjacent to the interface) surfactant concentrations given by C and C_s, respectively, are scaled on the initial bulk surfactant concentration, C_∞. As a result of this scaling, the dimensionless equations read

$$\nabla \cdot \tilde{\mathbf{u}} = 0, \tag{2.2}$$

$$\tilde{\rho}\left(\frac{\partial \tilde{\mathbf{u}}}{\partial \tilde{t}} + \tilde{\mathbf{u}} \cdot \nabla \tilde{\mathbf{u}}\right) + \nabla \tilde{p} = -Bo\mathbf{i}_z + Oh\, \nabla \cdot \left[\tilde{\mu}(\nabla \tilde{\mathbf{u}} + \nabla \tilde{\mathbf{u}}^T)\right] + \int_{\tilde{A}(\tilde{t})} (\tilde{\sigma}\tilde{\kappa}\mathbf{n} + \nabla_s \tilde{\sigma})\delta\left(\tilde{\mathbf{x}} - \tilde{\mathbf{x}}_f\right) \mathrm{d}\tilde{A}, \tag{2.3}$$

$$\frac{\partial \tilde{C}}{\partial \tilde{t}} + \tilde{\mathbf{u}} \cdot \nabla \tilde{C} = \frac{1}{Pe_b} \nabla^2 \tilde{C}, \tag{2.4}$$

$$\frac{\partial \tilde{\Gamma}}{\partial \tilde{t}} + \nabla_s \cdot (\tilde{\Gamma} \tilde{\mathbf{u}}_\mathrm{t}) = \frac{1}{Pe_s} \nabla_s^2 \tilde{\Gamma} + Bi \left(k\tilde{C}_s(1 - \tilde{\Gamma}) - \tilde{\Gamma}\right), \tag{2.5}$$

$$\tilde{\sigma} = 1 + \beta_s \ln\left(1 - \tilde{\Gamma}\right), \tag{2.6}$$

where the density and viscosity are given by $\tilde{\rho} = \rho_g/\rho + (1 - \rho_g/\rho)\,\mathcal{H}\left(\tilde{\mathbf{x}}, \tilde{t}\right)$ and $\tilde{\mu} = \mu_g/\mu + (1 - \mu_g/\mu)\,\mathcal{H}\left(\tilde{\mathbf{x}}, \tilde{t}\right)$ wherein $\mathcal{H}\left(\tilde{\mathbf{x}}, \tilde{t}\right)$ represents a smoothed Heaviside function, which is zero in the gas phase and unity in the liquid phase, while the subscript g designates the gas phase; $\tilde{\mathbf{u}}_\mathrm{t} = (\tilde{\mathbf{u}}_\mathrm{s} \cdot \mathbf{t})\,\mathbf{t}$ is the tangential velocity at the interface in which $\tilde{\mathbf{u}}_\mathrm{s}$ represents the interfacial velocity; κ is the curvature; $\nabla_s = (\mathbf{I} - \mathbf{nn}) \cdot \nabla$ is the interfacial gradient wherein $\mathbf{I}$ is the identity tensor and $\mathbf{n}$ is the outward-pointing unit normal; δ is the Dirac delta function, which is equal to unity at the interface, located at $\tilde{\mathbf{x}} = \tilde{\mathbf{x}}_f$, and zero otherwise; $\tilde{A}(\tilde{t})$ is the time-dependent interface area.

The dimensionless groups that appear in the above equations are defined as

$$Bo = \frac{\rho g R_o^2}{\sigma_s}, \quad La = \frac{1}{Oh^2} = \frac{\rho \sigma_s R_o}{\mu^2}, \tag{2.7}$$

$$Bi = \frac{k_d R_o}{U}, \quad k = \frac{k_a C_\infty}{k_d}, \quad Pe_s = \frac{U R_o}{D_s}, \quad Pe_b = \frac{U R_o}{D_b}, \quad \beta_s = \frac{\Re T \Gamma_\infty}{\sigma_s}, \tag{2.8}$$

where Bo stands for the Bond number and represents the ratio of gravitational to capillary forces; $Oh = \mu/\sqrt{\rho \sigma_s R_o}$ is the Ohnesorge number that measures the relative importance of viscous to surface tension forces, and La is the Laplace number; Bi denotes the Biot number representing the ratio of characteristic desorptive to convective time-scales; k is the ratio of adsorption to desorption time scales; Pe_s and Pe_b are the interfacial and bulk Peclet numbers, respectively, and represent the ratio of convective to diffusive time-scales in the plane of the interface and the bulk, respectively; and β_s is the surfactant elasticity number, which measures the sensitivity of the surface tension to the surfactant concentration. The parameter $\mathcal{R}$ refers to the thermodynamic ideal gas constant value 8.314 J K^{-1} mol^{-1}. In addition to the above parameters, we assume an initially uniform surfactant concentration at the interface so that $\Gamma(\mathbf{x}, t = 0) = \Gamma_o = \Gamma_\infty/4$. The chosen density and viscosity ratios, $\rho_g/\rho = 1.2 \times 10^{-3}$ and $\mu_g/\mu = 0.018$, respectively, are representative of an air-water system.

The Marangoni stress, $\tilde{\tau}$, is expressed as a function of $\tilde{\Gamma}$:

$$\tilde{\tau} \equiv \nabla_s \tilde{\sigma} \cdot \mathbf{t} = -\frac{\beta_s}{1 - \tilde{\Gamma}} \nabla_s \tilde{\Gamma} \cdot \mathbf{t}, \tag{2.9}$$

where $\mathbf{t}$ is the unit tangent to the interface; tildes are dropped henceforth. From equation 2.9, the variation of τ can be achieved by altering the elasticity parameter, the magnitude of the interfacial concentration or the interfacial concentration gradients. In the current study, the weakening or strengthening of the Marangoni stresses have been analysed by studying the variation of β_s. The Marangoni time-scale, $\mu R_o/\Delta\sigma = O(10^{-5})$ s, as compared to the capillary and sorptive time-scales, which are of order $O(10^{-4})$ s and $O(10^{-3} - 10^{-5})$ s, respectively ; thus Marangoni stresses will play a key role in the dynamics.

The numerical procedure to solve equations (2.2)-(2.6) has been presented in detail by Shin *et al.* (2017, 2018); only a brief summary is provided here. The Navier-Stokes equations are solved by using a finite-volume method over a staggered grid (Harlow & Welch 1965). The computational domain comprises of a fixed regular grid (i.e. Eulerian grid) in which the spatial derivatives are approximated by standard centred-difference discretisation, except for the non-linear term, which is discretised using a second-order essentially non-oscillatory (ENO) scheme (Shu & Osher 1989). The projection method presented by Chorin (1968) is used to enforce the incompressibility behaviour.

The interface is tracked by an additional Lagrangian grid by using the front-tracking method and regularly reconstructed by a level-set method. The immersed boundary method of Peskin (1977) is used for communication between both grids. The temporal integration scheme is based on a second-order Gear method. Thus, even though our method as described in Shin & Juric (2002, 2009) follows a hybrid level-set/front-tracking approach, incorporating some features of level-sets, it is important to note that it fully retains the well-established Immersed Boundary formulation for surface forces used in the front-tracking method, which requires the surface integral representation in Eq. (2.3). The mathematical apparatus is detailed in the pioneering work of Peskin (1977). Finally, surfactant transport is solved on the interface, where the interfacial surfactant

concentration is located on the centre of the triangular front elements. More information can be found in Shin *et al.* (2017, 2018).

2.1. *Numerical setup, validation, and parameters*

The dimensionless computational domain size is chosen as $(15R_o)^3$, which is found to be sufficiently large to render boundary effects negligible. Hence a radial component is defined as $r = \sqrt{(x-x_o)^2 + (y-y_o)^2}$ where x_o and y_o are the abscissa and ordinate bubble position, respectively. Solutions are sought subject to Neumann boundary conditions on all variables at the lateral boundaries, $p = 0$ at the top boundary $z = 15R_o$, and no-slip at $z = 0$. At the free surface, we impose $\mathbf{n} \cdot \nabla \tilde{C} = -BiPe_b \left(k\tilde{C}_s(1-\tilde{\Gamma}) - \tilde{\Gamma} \right)$ as a condition on $\tilde{C}$ (more information can be found in Shin *et al.* (2018)). Simulations are initialised as a bubble resting immediately beneath the free surface before its rupture. Its initial shape is determined by solving the Young-Laplace equation for $Bo = 10^{-3}$, which is sufficiently small to avoid the effect of gravity on the bubble bursting process. To initialise bursting, the top spherical cap of the bubble is removed, leaving only a bubble cavity (see figure 1a). The relevant time scale associated with the cap-retraction , $t_{CR} = R_o/\sqrt{2\sigma/\rho\delta} = O(10^{-6})$s, is too short to affect the dynamics. A similar approach has been used by Boulton-Stone & Blake (1993), Garcia-Briones *et al.* (1994), Duchemin *et al.* (2002) and Deike *et al.* (2018). Our numerical simulations have been validated against the work of Eggers (1993) and Lai *et al.* (2018) in terms of liquid thread breakup, and the scaling of the ejected jet length, L_d, with La (see figure 1b), respectively. Solving the small-scales of the bursting dynamics is a challenging process. We have assessed the grid dependence of our results ensuring their convergence for grids larger than 768^3.

In the current study, the Laplace number has been fixed to $La = 2 \times 10^4$ following the works of Lai *et al.* (2018) and Gordillo & Rodríguez-Rodríguez (2019). Additionally, we have set the Bond number Bo to be of $O(10^{-3})$ to ensure that the shape of the bubble prior to its rupture is spherical even in the presence of surfactants. Operating in this parameter space allows for the elimination of gravitational effects and the isolation of Marangoni-induced dynamics during jet-drop formation. As mentioned earlier, to study the effect of Marangoni stresses on the flow, we have varied the elasticity parameter in the range of $0.7 < \beta_s < 0.9$. In the context of this work, both the superficial and bulk Peclet numbers are set to unity, making neither the diffusion nor the convective terms dominant. With respect to the solubility, we have studied the range $10^{-2} < Bi < 10^0$, where for the lower end of the parameter scale the sorptive timescales are much larger than those associated with interfacial effects, and the dynamics are expected to be similar to those observed for an insoluble surfactant case, whereas for the upper end, surfactants tend to desorb from the interface and the dynamics begin to resemble those of a surfactant-free case. In summary, we have chosen the values of the surfactant-related parameters to ensure that all of the relevant physical processes associated with surfactant transport such as Marangoni stresses, surface/bulk diffusion, and sorption kinetics are represented in the present study.

3. Results

3.1. *Bursting bubble dynamics of the surfactant-laden base case*

The spatio-temporal evolution of the interfacial dynamics, shown in figure 2, is considered for the case characterised by $La = 2 \times 10^4$, $Bo = 10^{-3}$, $Pe_s = 1$, $\beta_s = 0.9$, $Bi = 0.01$, $k = 1$, and $\Gamma_o = k/4$. At early times, a large capillary pressure is generated

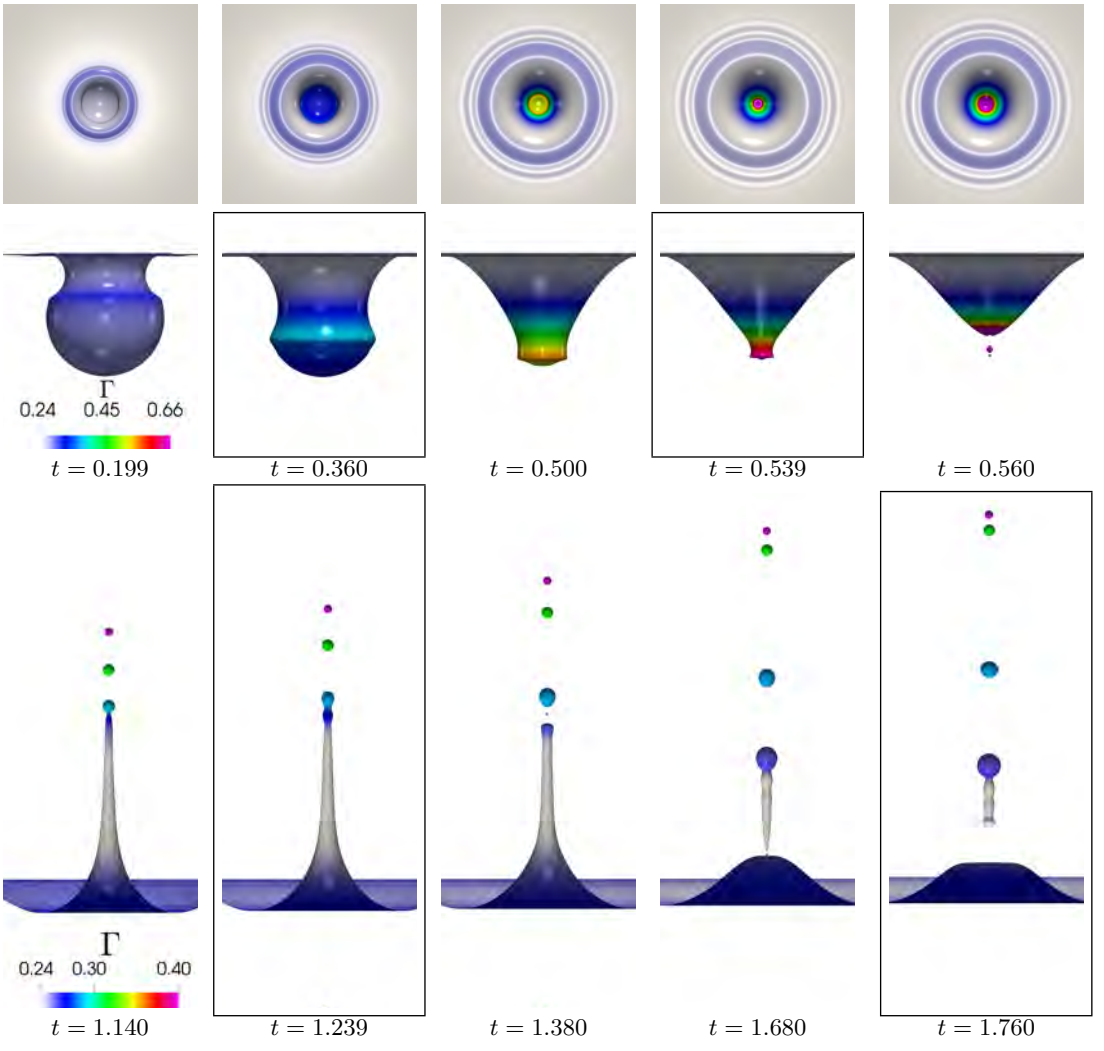

FIGURE 2. Spatio-temporal evolution of the dynamics of the interface and of the interfacial surfactant concentration, Γ, with $La = 2 \times 10^4$, $Bo = 10^{-3}$, $Pe_s = 1$, $\beta_s = 0.9$, $Bi = 0.01$, $k = 1$, and $\Gamma_o = k/4$. The colour bars indicate the magnitude of Γ. Top row: top-view of the interface; middle row: side-view of cavity collapse; bottom row: Worthington jet (entrapped bubble is not shown).

near the nucleated hole due to the high curvature of the interface joining the spherical bubble and the horizontal free surface. This capillary pressure leads to rapid expansion of the hole and the creation of a toroidal capillary wave, which travels toward the bottom of the bubble. The convergence of this wave on the bubble rear leads to the formation of a cusp-like region, which is relieved via the detachment of downward-moving conical bubbles, and the formation of a vertical, upward-directed, high-speed, Worthington jet. Small droplets are subsequently ejected from the tip of the jet, triggered by a Rayleigh-Plateau instability. A pinchoff event is also seen to occur at the base of the Worthington jet that leads to retraction of the emitted ligament into a spheroidally-shaped drop.

In figure 3, we show snapshots of the interface, the interfacial concentration, Γ, the Marangoni stress, τ, the interfacial tangent velocity component, u_t, that provides a

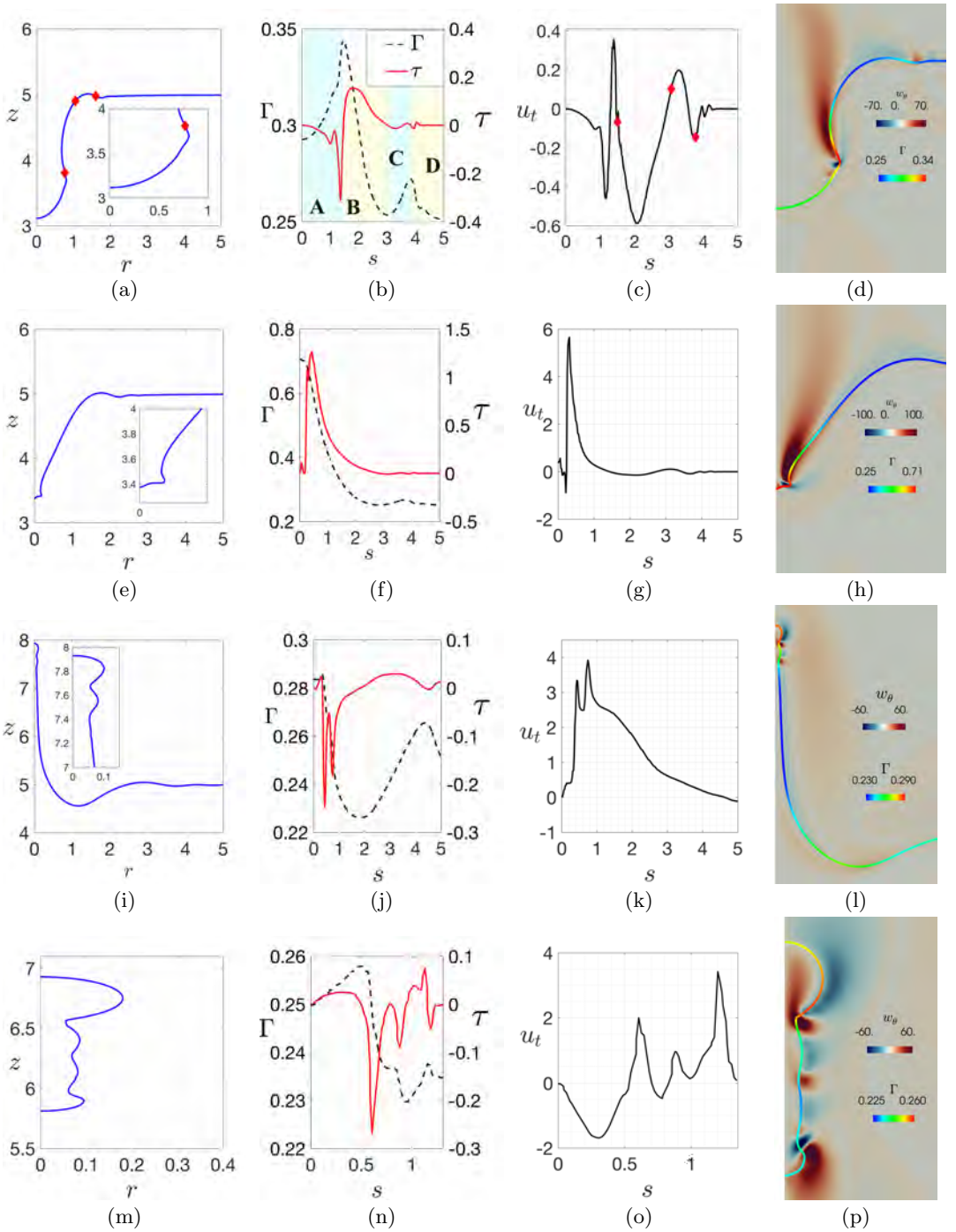

FIGURE 3. Interface location, Γ and τ, u_t, and ω_θ are shown in columns one to four, respectively. In columns 1,4 and 2,3, the variation is with respect to the dimensionless radial coordinate, r, and arc length, s, respectively. Panels (a)-(d), and (e)-(h) show the cavity collapse dynamics $t = 0.360$ and $t = 0.539$, respectively, (i)-(l) the Worthington jet at $t = 1.239$, and (m)-(h) the retracting ligament at $t = 1.760$. The insets in (e) and (i) respectively focus on the bottom of the collapsing cavity, and the oscillations at tip of the Worthington jet that will eventually lead to its breakup. A description of regions 'A'-'D' in (b) is provided in the text. The parameter values are the same as in figure 2.

measure of mobility, and the azimuthal component of the vorticity, ω_θ. These snapshots, which are taken at $t = 0.360$, 0.539, 1.239, and 1.760, corresponding to the framed panels in figure 2, reflect the strong coupling between these flow variables. Figure 3a,b illustrates that the collapsing cavity, and the accompanying capillary wave, transport surfactant towards the bottom of the bubble giving rise to a local decrease in surface tension. It is also instructive to separate figure 3b into four regions due to the existence of stagnation points. In region 'A', $\tau < 0$ and $u_t < 0$, indicating that the direction of the Marangoni flow is towards the bottom of the bubble, which aids cavity collapse and surfactant transport in this direction. In region 'B', $\tau > 0$ and $u_t > 0$, thus the Marangoni flow is directed away from the origin, which retards the collapse process. A similar behaviour is seen in regions 'C' and 'D' in which the trailing edge of the capillary wave has a similar Γ distribution, albeit with a smaller magnitude, to its leading edge. As a result, $\tau < 0$ and $\tau > 0$, and $u_t < 0$ and $u_t > 0$ in regions 'C' and 'D', which drives flow towards the bottom of the bubble and its tail, respectively. Figure 3b,c also shows the existence of an interfacial stagnation point ($s \sim 1.4$), where surfactant accumulates, Γ is highest, and the magnitude of τ is largest. This occurs in the region where ω_θ changes sign as the stagnation point is created (see figure 3d) corresponding to the capillary wave moving towards the bottom of the bubble.

Figure 3e-h shows the dynamics at $t = 0.539$ prior to the cavity collapse. The stagnation point where the surfactant accumulates has moved downward to the bottom of the cavity and the magnitude of ω_θ has increased in comparison to that in figure 3d. The interfacial surfactant concentration reaches its maximum value as the surfactant-laden capillary wave converges on the flow origin. The Marangoni stresses drive motion from high to low Γ regions and therefore act to oppose the flow, as indicated by the fact that both $\tau > 0$ and $u_t > 0$ over the majority of the spatial domain except in the close vicinity of the bottom of the cavity.

Figure 3i shows a snapshot of the jet for $t = 1.239$ in a situation of pinch-off 'escape' with a bulbous region formed at its tip. From figure 3j, we observe that Γ has two peaks: one at the jet tip, and a lower one far upstream. Figure 3l also shows that the change in the sign of ω_θ is linked to the Γ distribution in the bulbous region. The associated τ distribution is such that $\tau < 0$ between the bottom of the jet and close to the bulbous region at the jet tip (that is for $0.4 < s < 1.9$), and $\tau > 0$ elsewhere including in the bulbous region. Flow is driven by capillarity from this region towards the quasi-cylindrical jet body and, from figure 3k, it is seen that $u_t > 0$ over the whole domain. This suggests that Marangoni stresses oppose this capillary-induced motion driving flow from the bottom of the jet towards the bulbous region. When these stresses are not sufficiently strong to overcome the Rayleigh-Plateau instability, an ejection of a droplet occurs after the pinch-off of the jet tip. The first drops detached from the tip are characterised by high interfacial concentration while successive droplet detachments have lower Γ, as demonstrated in figure 2 for $t \geqslant 1.114$.

At $t = 1.680$ (see figure 2), the Worthington jet pinches off from its base forming an elongated ligament thread. Capillary waves develop on the ligament surface, leading to interfacial oscillations as the detached ligament transitions to a spherical drop. In figure 3m-p, we have isolated the retracting ligament shown at $t = 1.760$ from the rest of the flow. In figure 3o, we observe the formation of four stagnation points at $s = 0$ 0.55, 0.7, and 0.84, which are connected to the change in the distributions of Γ and τ. From figure 3n,o, it is also seen that the Marangoni stresses oppose ligament pinchoff since $\tau > 0$ and $u_t < 0$ ($\tau < 0$ and $u_t > 0$) for $0 \leqslant s \leqslant 0.55$ ($0.55 \leqslant s \leqslant 0.7$). For $0.7 \leqslant s \leqslant 0.84$ ($s > 0.84$), the Marangoni stresses oppose (aid) the stretching of the ligament as $\tau < 0$ and $u_t > 0$ ($\tau > 0$ and $u_t > 0$). Close inspection of ω_θ (see figure 3p) reveals that high

vorticity production is observed close to the first stagnation point, which corresponds to the ligament 'neck'. As shown by Constante-Amores *et al.* (2020), the presence of such high vorticiy regions near the neck is a requirement for the Marangoni-driven inhibition of capillary-induced 'end-pinching' of retracting surfactant-laden ligaments.

Figure 4a shows the temporal evolution of the jet-tip from the moment after the ejection of a jet-droplet to its next capillary singularity. The formation of a bulbous edge on the jet-tip is driven by capillarity (at $t = 1.120$). The estimated Oh number for the tip, using the jet radius as a reference, is $Oh \approx 0.02$. Therefore, we are still in the region of low Oh number, and consequently, the inhibition of the 'end-pinching' mechanism, identified by Constante-Amores *et al.* (2020) can be invoked in order to rationalise the flow behaviour in this case. By close inspection of τ and u_{tr} (the radial component of the tangential velocity u_t), it is possible to identify that Marangoni-induced flow prevents the capillary breakup and reopens the neck of the jet-tip ($t = 1.140$). The reason behind the reopening of the neck is the suppression of the stagnation point close to the neck due to the Marangoni-induced flow brought about by the surfactants (see figure 4d). As was shown by Constante-Amores *et al.* (2020), two stagnation points close to the neck are necessary for capillary breakup to occur (see figure 4e).

In order to isolate the surface tension-reducing effects of surfactants from those associated with Marangoni stress-formation, we show in figure 5a snapshots of the interface at $t = 0.44$, 0.496, and 0.500 for the surfactant-free, surfactant-laden but Marangoni-suppressed, and full-Marangoni cases, respectively, prior to cavity-collapse for the same parameters as in figure 3. These times were chosen at identical spatial locations of the bubble rear in the axis of symmetry ($z \sim 3.28$). For the Marangoni-suppressed case, the reduced surface tension value is calculated via replacing Γ by Γ_o in equation 2.6. The presence of surfactant has been shown to enhance capillary wave-damping by Asaki *et al.* (1995) due to the interfacial rigidification brought about by τ, and this is seen clearly in figure 5a: the size of the cavity is largest for the full-Marangoni case, at the same stage of the dynamics for the three cases considered.

The capillary pressure field shown in figure 5b,c for the surfactant-free and full-Marangoni cases is influenced heavily by the capillary pressure and, therefore, the local interfacial curvature and surface tension. From panels (b) and (c) of figure 5, it is seen that the pressure is highest immediately upstream of the capillary wave peak and this pressure gradient drives flow towards the lower-pressure region located at bottom of the cavity that coincides with the axis of symmetry. Furthermore, Marangoni stresses induce a recirculation zone close to the free surface as shown in figure 5c. In figure 5d, we also show the axial distribution of the pressure at the axis of symmetry and this displays a peak at the interface due to capillarity. Owing to the presence of surfactant, the surface tension is reduced, which leads to a concomitant fall in the pressure, as illustrated via comparison of figure 5b,c. The pronounced reduction in capillary pressure, due primarily to the accumulation of surfactant at the bottom of the cavity, is shown in figure 5d.

As mentioned above, the convergence of the capillary wave on the bottom of the cavity leads to the formation of a Worthington jet (Gordillo & Rodríguez-Rodríguez 2019), which is shown in figure 5e for the surfactant-free, Marangoni-suppressed, and full-Marangoni cases for $t = 0.507$, $t = 5.94$, and $t = 0.619$, respectively; again, these times are chosen at nearly identical spatial locations of the jet tip in the axis of symmetry. The larger pressure gradient associated with the surfactant-free case, discussed above, leads to longer jets, with more pronounced bulbous regions at their tips, in comparison to the full-Marangoni case where the retarding Marangoni stresses induce a recirculation zone close to the jet-base. Close inspection of figure 4e also reveals that the longest jets are associated with the $\tau = 0$ (rather than the surfactant-free) case wherein there is no

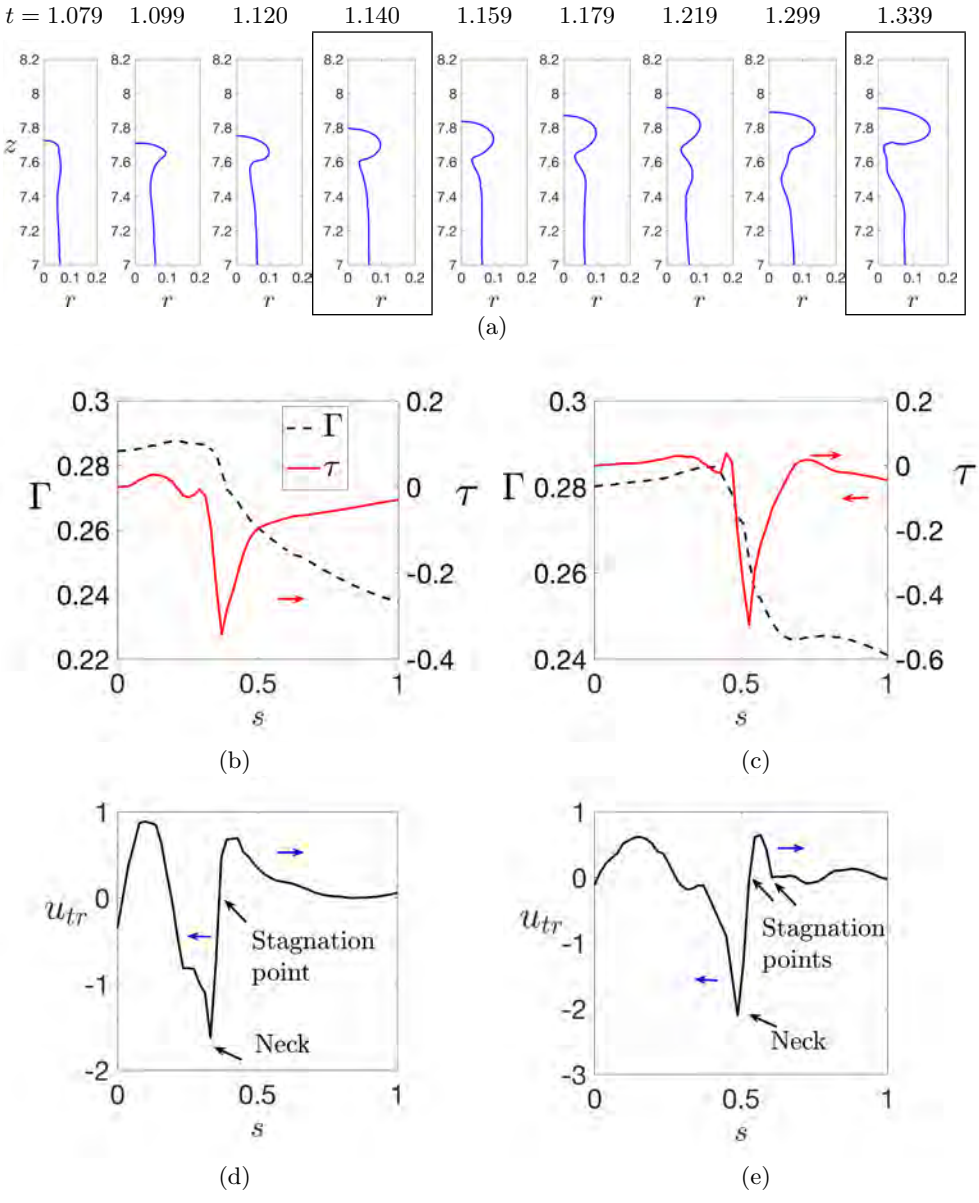

FIGURE 4. (a) Spatio-temporal evolution of the jet-tip and its escape from pinchoff for the surfactant-laden base case. Panels (b) and (c) represent Γ and τ on the arc length s for time $t = 1.140$ and 1.339, respectively; (d) and (e) represent the radial component of the tangential velocity u_{tr} as a function of the arc length s, respectively. The red arrows in (b) and (c) represent the direction of Marangoni-induced flow, and the blue arrows in (d) and (e) highlight the direction of the flow driven by capillarity. The value $s = 0$ corresponds to the tip of the jet at $r = 0$. The parameter values are the same as in figure 2.

Marangoni-induced retardation and for which La is lowest. As shown previously (Lai *et al.* 2018), decreasing La leads to faster, and thinner jets, with a greater propensity for breakup. As a result, a reduction in the number of ejected droplets is observed for the shorter, and slower, full-Marangoni jets: four (see figure 2), seven, and nine droplets (the latter two not shown) for the full-Marangoni, surfactant-free, and Marangoni-suppressed

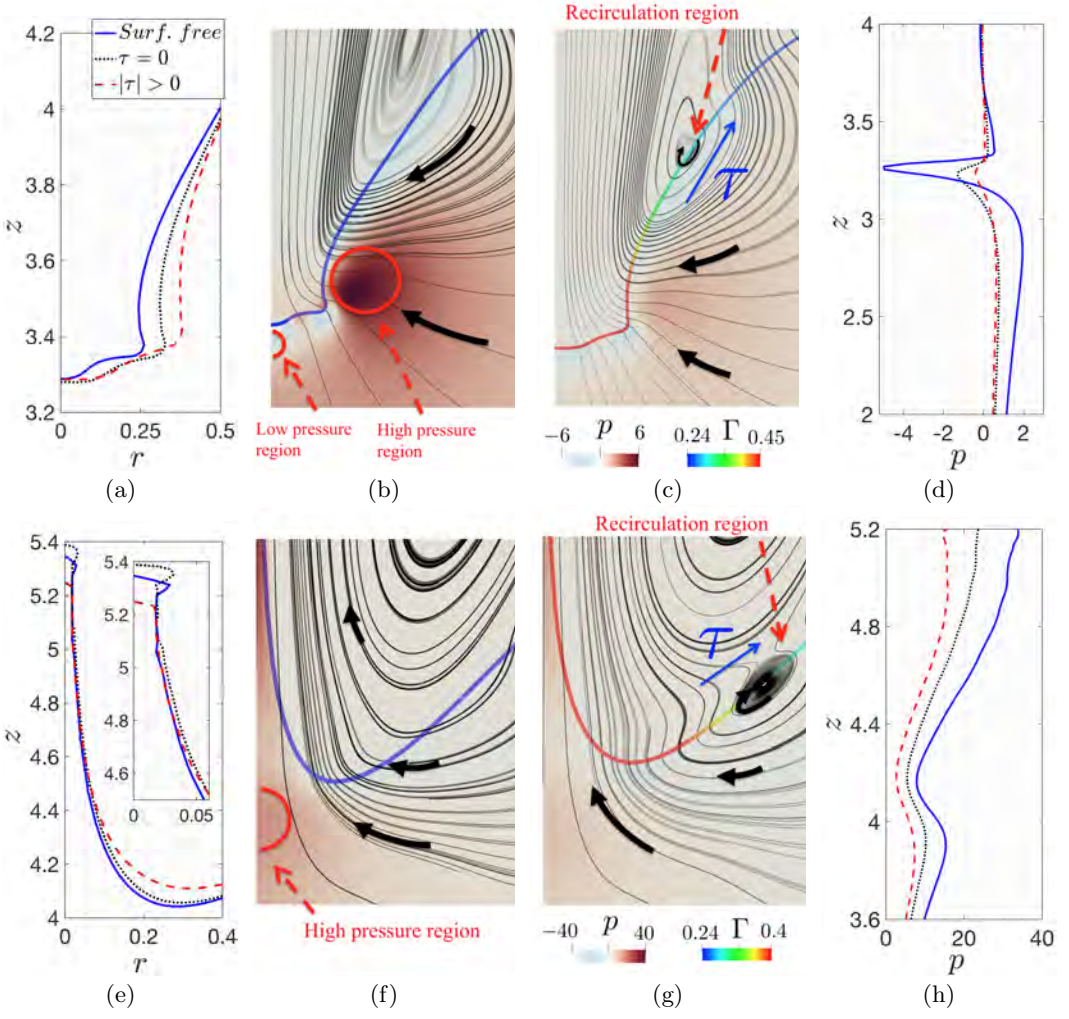

FIGURE 5. Interface location, pressure field together with a representation of the streamlines for the surfactant-free and full-Marangoni ($|\tau| > 0$) cases, and pressure on the axis of symmetry, are shown in columns one to four, respectively. Panels (a-d) and (e-h) show the cavity collapse dynamics (at $t = 0.440$, 0.496, and 0.500, for the surfactant-free, no-Marangoni [$\tau = 0$], and full-Marangoni cases) and the Worthington jet (at $t = 0.507$, 0.594, and 0.619, for the surfactant-free, $\tau = 0$, $|\tau| > 0$ cases), respectively. The parameter values are the same as those used to generate figure 2.

cases, respectively. The droplet numbers for surfactant free and Marangoni-suppressed cases agree with Berny *et al.* (2020). Finally, as shown in figure 5h, there is an adverse pressure gradient in all cases, since capillarity drives flow from the bulbous region towards the jet base, which is largest for the surfactant-free case.

The immobilising effect of the Marangoni stresses can be seen in figure 6a in which we plot the kinetic energy, defined as $E_k = \int_V (\rho \mathbf{u}^2/2) dV$, where Marangoni stresses reduce the maximal and asymptotic values of E_k in comparison to the surfactant-free and no-Marangoni cases. In figure 6b, we observe further that the motion of the interface is retarded maximally when Marangoni stresses are enabled fully. Inspection of figure 6c also reveals that the interfacial area A, normalised by its initial value, A_o, reduces over time leading to large Γ at the moment of interfacial vertical collapse at $t \sim 0.550$.

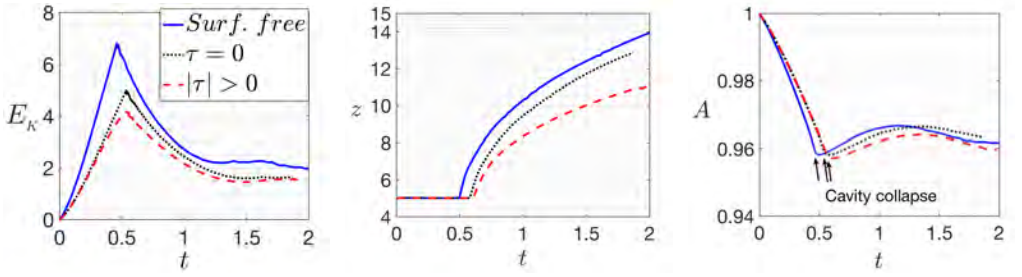

FIGURE 6. Temporal evolution of kinetic energy, the maximal vertical interface location, and interfacial area (normalised by its initial value), (a)-(c), respectively, for the surfactant-free, full-Marangoni, and no-Marangoni cases, for the same parameters as in figure 2.

TABLE 1. Droplet characteristics of surfactant-laden case

Droplet Number	V/V_o	Γ
1	2.374×10^{-4}	0.406
2	6.643×10^{-4}	0.307
3	2.279×10^{-3}	0.285
4	8.875×10^{-3}	0.247

We have measured the droplet characteristics, in terms of their volume and their average interfacial surfactant concentration, at time $t = 1.76$, as shown in figure 2, and summarised the results in the table 1. The droplets are numbered depending on the order of ejection from the tip of the jet (i.e. the highest droplet in the computational domain corresponds to the first ejected droplet). The volume of each droplet is normalised with the initial volume of the spherical bubble. This shows the multi-scale nature of the phenomenon. Moreover, the size of the first droplet, $r_d/R_o \sim 6\%$, which agrees with the experimental observations of Blanchard & Woodcock (1957) and Tedesco & Blanchard (1979), the empirical power law-dependence of Lewis & Schwartz (2004), and the theoretical scaling relationship proposed by Gañán-Calvo (2017). The predicted surfactant concentration of the ejected droplets is higher in value than the concentration of the liquid reservoir. This agrees with the experimental studies of Blanchard & Syzdek (1972) which were carried out within the context of examining bacterial concentrations in bursting bubbles.

3.2. *Parametric study*

Here, we investigate the effect of system parameters on the dynamics of the bursting phenomenon beginning with the influence of β_s which controls the relative strength of Marangoni stresses. As shown previously, the presence of surfactant tends to rigidify the interface and delays the cavity collapse (see figure 7a). By increasing β_s, Marangoni stresses are strengthened leading to greater rigidification of the interface, and consequently, higher retardation of the cavity collapse (see figure 7a). This collapse-retardation is also accompanied by a lower surfactant convection towards the point of singularity (see figure 7c). Moreover, the strengthening of Marangoni stresses via increase in β_s leads to dampening of the tangential velocity along the interface (see figure 7e), o thinner jets,

and fewer ejected droplets (e.g. seven and four droplets for the lower and upper ends of the elasticity parameter β_s).

We also analyse the effect of surfactant solubility on the bursting dynamics by varying the value of the Biot number, Bi. For the lower Bi values, the sorptive time-scales are larger than those associated with the interfacial dynamics and the Marangoni stresses, and consequently, the system behaves as if the surfactant were effectively insoluble. From the representation of the interfacial location of the cavity, we see that the desorptive time-scales dominate the system and, consequently, a reduction of Γ is observed as Bi increases (see figure 8a) with a concomitant weakening of the Marangoni stresses which oppose cavity collapse. The increase in interfacial mobility, characterised by a rise in the magnitude of u_t is also seen in figure 8e.

We also examine the effect of solubility on the jet dynamics whereupon we observe that at the lower end of the Biot number, the jet is slowest due to interfacial rigidification brought about by τ, as can be seen via the damping of u_t, shown in figure 8f. Higher gradients in Γ are observed for weakly-soluble case (see figure 8d), which leads to the highest strength of τ. With increasing Bi more interfacial surfactants migrate to the bulk and as a result gradients in Γ are reduced, leading to an overall weakening of the Marangoni stresses. Finally, we study the effect of solubility on the number of ejected droplets. As before, the desorption of surfactant from the interface as Bi increases yields weakening of τ and, subsequently, the surfactant does not prevent 'end-pinching' of the jet-tip from which a larger number of droplets are ejected than in the low Bi case; for $Bi = 1$, seven droplets are ejected in comparison with the four droplets produced by the weakly-soluble case characterised by $Bi = 0.01$.

4. Concluding remarks

The effect of Marangoni-induced flow, brought about by the presence of surfactant, on the dynamics of a bubble bursting through an interface was studied using a hybrid front-tracking/level-set method. Our results indicate that a surfactant-covered toroidal capillary wave forms, following the collapse of the cavity, whose motion is retarded by the surfactant-induced Marangoni stresses; these stresses drive flow from regions of high surfactant concentration (low surface tension) to low concentration (high tension) regions. The immobilising effect of the surfactants due to the Marangoni stresses is also observed via the marked reduction in the system kinetic energy and the generation of shorter, and slower, Worthington jets. The breakup of these jets is accompanied by the formation of fewer droplets in comparison to the surfactant-free case. This behaviour is associated with the 'end-pinching' mechanism of the jet-tip and the presence of surfactant promotes the neck re-opening through Marangoni-flow, induced by the formation of surfactant concentration gradients, and not only via lowering of the mean surface tension value. Finally, we have examined the role of the elasticity number β_s which is an important parameter that controls the strengthening or weakening of Marangoni stresses along the interface. An increase in β_s leads to a reduction in tangential velocity, and consequently a retardation in interfacial motion. In a similar way, the surfactant solubility, via the variation of Biot number Bi, was also examined in this study. An increase in this parameter leads to a rise in the rate of mass transfer from the bulk to the interface resulting in the overall weakening of Marangoni stresses, and consequently, a larger number of droplets as Marangoni stresses cannot prevent the 'end-pinching' mechanism from the jet-tip.

Future research avenues for study are to perform numerical simulations featuring three dimensional behaviours occurring for large Bond numbers ($Bo \geqslant 0.5$). It has been

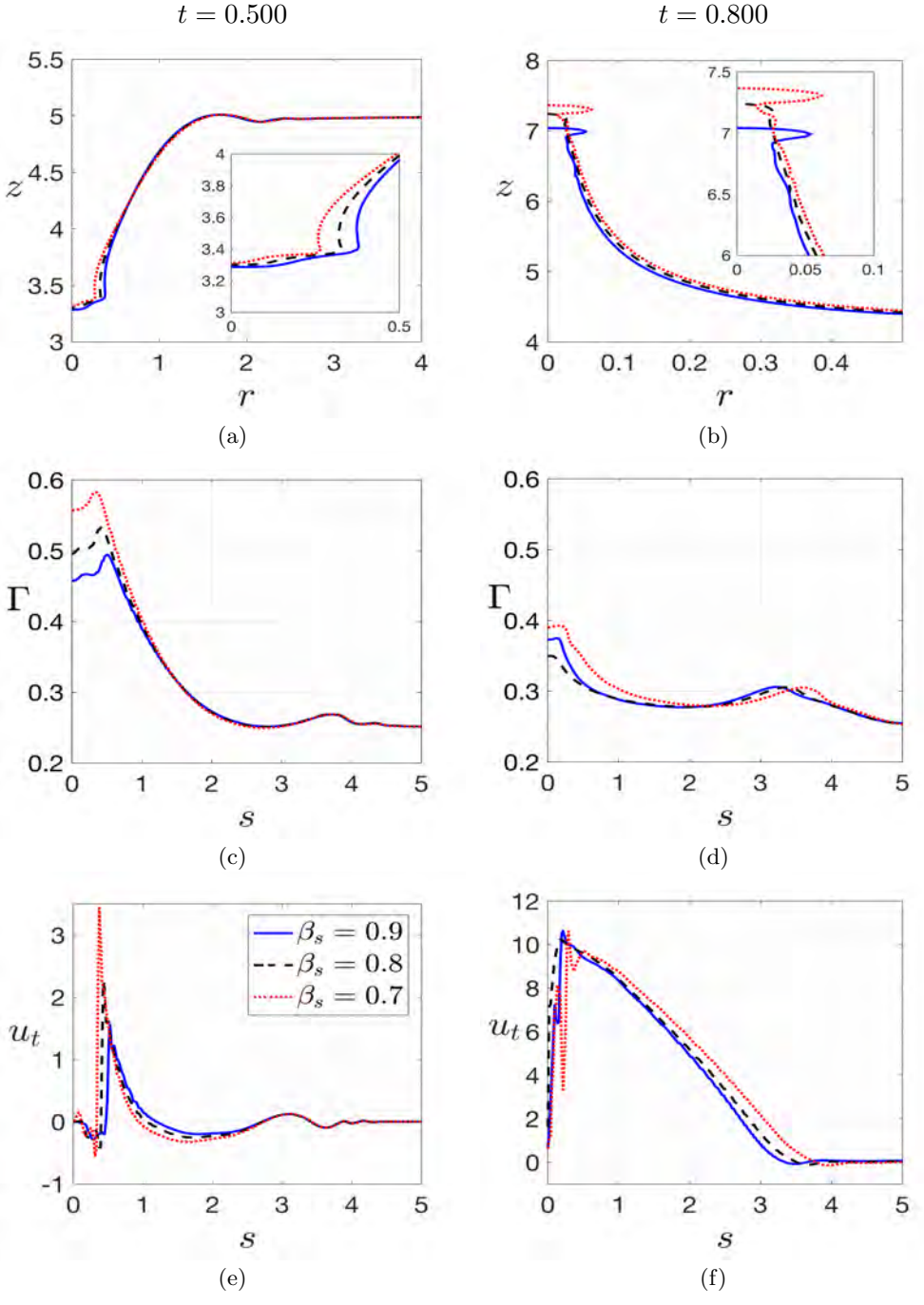

FIGURE 7. Effect of the elasticity number, β_s, on the bursting dynamics for $La = 2 \times 10^4$, $Bo = 10^{-3}$, $Pe_s = 1$, $Bi = 0.01$, $k = 1$ and $\Gamma_o = 1/4$. Panels (a) and (b) represent the interfacial shape, (c) and (d) the interfacial surfactant concentration Γ along the arc length s, and (e) and (f) the tangential velocity u_t along s, during the cavity collapse at $t = 0.500$ and the Worthington jet at $t = 0.800$, respectively.

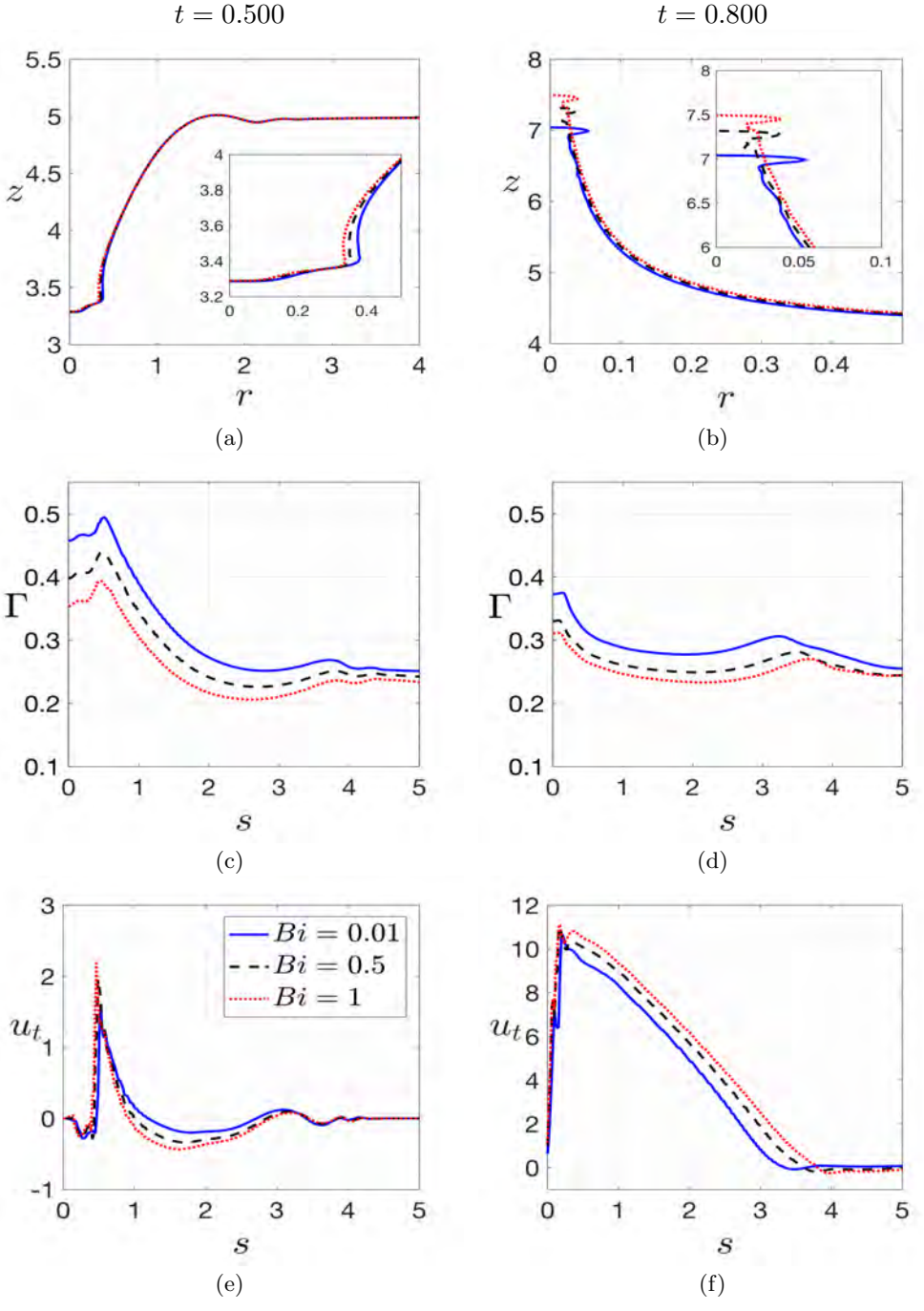

FIGURE 8. Effect of the Biot number, Bi, on the bursting dynamics for $La = 2\times10^4$, $Bo = 10^{-3}$, $Pe_s = 1$, $\beta_s = 0.9$, $k = 1$ and $\Gamma_o = 1/4$. Panels (a) and (b) represent the interfacial shape, (c) and (d) the interfacial surfactant concentration Γ along the arc length s, and (e) and (f) the tangential velocity u_t along s, during the cavity collapse at $t = 0.500$ and the Worthington jet at $t = 0.800$, respectively.

shown by Ghabache (2015) that at large values of Bo, the bursting outcome can be either axisymmetric or purely three-dimensional producing an oblique Worthington jet. Both surfactant-free and surfactant-laden bubbles should be examined with a similar formulation to that described in Section 2. Thus, the bubble initialisation will require taking into account the entirety of the same: the immersed cavity, the cap, and the meniscus. If the hole formation is located anywhere else on the cap, a three-dimensional cap retraction will certainly affect the behaviour of the collapsing cavity to finally culminate in an inclined Worthington jet, and complex droplet detachment.

Declaration of Interests. The authors report no conflict of interest.

This work is supported by the Engineering & Physical Sciences Research Council (EPSRC), United Kingdom, through a studentship for C.R.C-A. in the Centre for Doctoral Training on Theory and Simulation of Materials at Imperial College London funded by the EPSRC (EP/L015579/1), and through the EPSRC MEMPHIS (EP/K003976/1) and PREMIERE (EP/T000414/1) Programme Grants. C.R.C-A also acknowledges the funding and technical support from BP through the BP International Centre for Advanced Materials (BP-ICAM), which made this research possible. O.K.M. also acknowledges funding from PETRONAS and the Royal Academy of Engineering for a Research Chair in Multiphase Fluid Dynamics, and the PETRONAS Centre for Engineering of Multiphase Systems. We also acknowledge HPC facilities provided by the Research Computing Service (RCS) of Imperial College London for the computing time. D.J. and J.C. acknowledge support through computing time at the Institut du Developpement et des Ressources en Informatique Scientifique (IDRIS) of the Centre National de la Recherche Scientifique (CNRS), coordinated by GENCI (Grand Equipement National de Calcul Intensif) Grant No. 2020A0082B06721. The numerical simulations were performed with code BLUE (Shin *et al.* 2017) and the visualisations have been generated using ParaView. We are grateful to the referees for many helpful and constructive comments.

REFERENCES

Asaki, T. J., Thiessen, D. B. & Marston, P. L. 1995 Effect of an insoluble surfactant on capillary oscillations of bubbles in water: observation of a maximum in the damping. *Phys. Rev. Lett.* **75** (14), 2686.

Berny, A., Deike, L., Séon, T. & Popinet, S. 2020 Role of all jet drops in mass transfer from bursting bubbles. *Phys. Rev. Fluids* **5**, 033605.

Blanchard, D. C. & Syzdek, L. D. 1972 Concentration of bacteria in jet drops from bursting bubbles. *Journal of Geophysical Research (1896-1977)* **77** (27), 5087–5099.

Blanchard, D. C. & Woodcock, A. H. 1957 Bubble formation and modification in the sea and its meteorological significance. *Tellus* **9** (2), 145–158.

Blanco-Rodrìguez, F. J. & Gordillo, J. M. 2020 On the sea spray aerosol originated from bubble bursting jets. *J. Fluid Mech.* **886**, R2.

Boulton-Stone, J. M. & Blake, J. R. 1993 Gas bubbles bursting at a free surface. *J. Fluid Mech.* **254**, 437–466.

Chorin, A. J. 1968 Numerical solution of the Navier-Stokes equations. *Mathematics of Computation* **22** (104), 745–745.

Constante-Amores, C. R., Kahouadji, L., Batchvarov, A., S., Seungwon, Chergui, J., Juric, D. & Matar, O. K. 2020 Dynamics of retracting surfactant-laden ligaments at intermediate ohnesorge number. *Phys. Rev. Fluids* **5**, 084007.

Craster, R. V., Matar, O. K. & Papageorgiou, D. T. 2002 Pinchoff and satellite formation in surfactant covered viscous threads. *Physics of Fluids* **14** (4), 1364–1376.

Craster, R. V., Matar, O. K. & Papageorgiou, D. T. 2009 Breakup of surfactant-laden jets above the critical micelle concentration. *Journal of Fluid Mechanics* **629**, 195–219.

Deike, L., Ghabache, E., Liger-Belair, G., Das, A. K., Zaleski, S., Popinet, S. & Séon, T. 2018 Dynamics of jets produced by bursting bubbles. *Phys. Rev. Fluids* **3**, 013603.

Duchemin, L., Popinet, S., Josserand, C. & Zaleski, S. 2002 Jet formation in bubbles bursting at a free surface. *Phys. Fluids* **14**, 3000.

Eggers, J. 1993 Universal pinching of 3d axisymmetric free-surface. *Phys. Rev. Lett.* **71**, 3458.

Gañán-Calvo, A. M. 2017 Revision of bubble bursting: Universal scaling laws of top jet drop size and speed. *Phys. Rev. Lett.* **119** (204502).

Garcia-Briones, M. A., Brodkey, R. S. & Chalmers, J. J. 1994 Computer simulations of the rupture of a gas bubble at a gas-liquid interface and its implications in animal cell damage. *Chem. Eng. Sci.* **49** (14), 2301–2320.

Ghabache, E. 2015 Out of equilibrium free surface: from cavity collapse to stretched jets. PhD thesis, Université Pierre et Marie - Paris VI.

Ghabache, E., Antkowiak, A., Josserand, C. & Séon, T. 2014 On the physics of fizziness: How bubble bursting controls droplets ejection. *Phys. Fluids* **26**, 121701.

Ghabache, E. & Séon, T. 2016 Size of the top jet drop produced by bubble bursting. *Phys. Rev. Fluids* **1**, 051901(R).

Gordillo, J. M. & Rodríguez-Rodríguez, J. 2019 Capillary waves control the ejection of bubble bursting jets. *J. Fluid Mech.* **867** (556–571).

Harlow, F. H. & Welch, J. E. 1965 Numerical calculation of time-dependent viscous incompressible flow of fluid with free surface. *The Physics of Fluids* **8** (12), 2182–2189.

Jin, F., Gupta, N. R. & Stebe, K. J. 2006 The detachment of a viscous drop in a viscous solution in the presence of a soluble surfactant. *Phys. Fluids* **18** (2), 022103.

Jin, F. & Stebe, K. J. 2007 The effects of a diffusion controlled surfactant on a viscous drop injected into a viscous medium. *Physics of Fluids* **19** (11), 112103.

Kamat, P. M., Wagoner, B. W., Thete, S. S. & Basaran, O. A. 2018 Role of marangoni stress during breakup of surfactant-covered liquid threads: Reduced rates of thinning and microthread cascades. *Phys. Rev. Fluids* **3**, 043602.

Kovalchuk, N. M., Jenkinson, H., Miller, R. & Simmons, M. J.H. 2018 Effect of soluble surfactants on pinch-off of moderately viscous drops and satellite size. *Journal of Colloid and Interface Science* **516**, 182 – 191.

Kovalchuk, N. M., Nowak, E. & Simmons, M. J. H. 2016 Effect of soluble surfactants on the kinetics of thinning of liquid bridges during drops formation and on size of satellite droplets. *Langmuir* **32** (20), 5069–5077.

Lai, C-Y., Eggers, J. & Deike, L. 2018 Bubble bursting: Universal cavity and jet profiles. *Phys. Rev. Lett.* **121**, 144501.

Lewis, E. R. & Schwartz, S. E. 2004 Sea salt aerosol production: Mechanisms, methods, measurements and models—a critical review. *Washington DC American Geophysical Union Geophysical Monograph Series* **152**, 3719–.

Lhuissier, H. & Villermaux, E. 2012 Bursting bubble aerosols. *J. Fluid Mech.* **696**, 5–44.

Liao, Y. C., Subramani, H. J., Franses, E. I. & Basaran, O. A. 2004 Effects of soluble surfactants on the deformation and breakup of stretching liquid bridges. *Langmuir* **20** (23), 9926–9930.

MacIntyre, F. 1972 Flow patterns in breaking bubbles. *J. Geophys. Res.* **77** (27), 5211–5228.

McGough, P. T. & Basaran, O. A. 2006 Repeated formation of fluid threads in breakup of a surfactant-covered jet. *Phys. Rev. Lett.* **96**, 054502.

Peskin, C. S. 1977 Numerical analysis of blood flow in the heart. *Journal of Computational Physics* **25** (3), 220 – 252.

Poulain, S. & Bourouiba, L. 2018 Biosurfactants change the thinning of contaminated bubbles at bacteria-laden water interfaces. *Phys. Rev. Lett.* **121**, 204502.

Séon, T. & Liger-Belair, G. 2017 Effervescence in champagne and sparkling wines: From bubble bursting to droplet evaporation. *Eur. Phys. J. Special Topics* **226**, 117–156.

Shin, S., Chergui, J. & Juric, D. 2017 A solver for massively parallel direct numerical simulation of three-dimensional multiphase flows. *J. Mech. Sci. Tech.* **31**, 1739–1751.

Shin, S., Chergui, J., Juric, D., Kahouadji, L., Matar, O. K. & Craster, R. V. 2018 A hybrid interface tracking – level set technique for multiphase flow with soluble surfactant. *J. Comp. Phys.* **359**, 409–435.

Shin, S. & Juric, D. 2002 Modeling three-dimensional multiphase flow using a level contour

reconstruction method for front tracking without connectivity. *J. of Comp. Phys.* **180**, 427–470.

Shin, S. & Juric, D. 2009 A hybrid interface method for three-dimensional multiphase flows based on front tracking and level set techniques. *Int. J. Num. Meth. Fluids* **60**, 753–778.

Shu, C. & Osher, S. 1989 Efficient implementation of essentially non-oscillatory shock-capturing schemes, ii. *Journal of Computational Physics* **83** (1), 32 – 78.

Singh, D. & Das, A. K. 2019 Numerical investigation of the collapse of a static bubble at the free surface in the presence of neighbors. *Phys. Rev. Fluids* **4**, 023602.

Tedesco, R. & Blanchard, D. 1979 Dynamics of small bubble motion and bursting in freshwater. *J. Rech. Atmos.* **13** (215).

Toba, Y. 1959 Drop production by bursting of air bubbles on the sea surface (ii) theoretical study on the shape of floating bubbles. *J. Ocean. Soc. Japan* **15** (3), 121–130.

Veron, F. 2015 Ocean spray. *Ann. Rev. of Fluid Mech.* **47**, 507–538.

Woodcock, A. H., Kientzler, C. F., Arons, A. B. & Blanchard, D. C. 1953 Giant condensation nuclei from bursting bubbles. *Nature* **172**, 1144–1145.

Zeff, B. W., Kleber, B., Fineberg, J. & Lathrop, D. P. 2000 Singularity dynamics in curvature collapse and jet eruption on a fluid surface. *Nature* **403**, 401–404.

Zenit, R. & Rodríguez-Rodríguez, J. 2018 The fluid mechanics of bubbly drinks. *Phys. Today* **71** (11), 44.